Enhanced light harvesting and electron-hole separation for efficient photocatalytic hydrogen evolution over Cu$_7$S$_4$-enwrapped Cu$_2$O nanocubes

Mengmeng Zhang[a], Zelin Chen[a], Yang Wang[a], Jinfeng Zhang[a], Xuerong Zheng[a], Dewei Rao[b], Xiaopeng Han[a], Cheng Zhong[a], Wenbin Hu[a], Yida Deng[a,*]

[a] School of Materials Science and Engineering, Key Laboratory of Advanced Ceramics and Machining Technology of Ministry of Education, Tianjin University, Tianjin, 300072, PR China
[b] School of Materials Science and Engineering, Jiangsu University, Zhenjiang, 212013, PR China

ABSTRACT

P-type Cu$_2$O is an advantageous photocatalyst as the appropriate bandgap structure and low-cost. However, poor photocatalytic and instability of such promising material is still a great challenge. Here the core-shell Cu$_7$S$_4$-coated Cu$_2$O nanocubes (Cu$_2$O/Cu$_7$S$_4$ NCs) were successfully synthesized by solution method coupled with anion exchange, and were firstly employed to hydrogen evolution reaction (HER). The resultant integrated structure of Cu$_2$O/Cu$_7$S$_4$ NCs exhibited apparent improved photocatalytic hydrogen evolution activity compared with Cu$_2$O photocatalyst. Particularly, Cu$_2$O/Cu$_7$S$_4$ NCs had a high hydrogen production rate of 1689.00 μmol g^{-1} h^{-1} under full spectra irradiation with additive of Na$_2$SO$_3$, which was higher than that of Cu$_2$O NCs with a factor of 1.71 times. Excellent synergistic effect of Cu$_2$O and Cu$_7$S$_4$ can be responsible for the improved hydrogen evolution properties, namely, the presence of Cu$_7$S$_4$ with localized surface plasma resonance (LSPR) can promote the photogenerated electrons transfer from the Cu$_2$O surface, prolong the photogenerated holes lifetime, accelerate the separation of photogenerated electrons and holes, and ameliorate the photoelectric properties of semiconductors. The in situ formed multifunctional Cu$_7$S$_4$ layer offers a promising avenue to design photocathodes rationally for photocatalytic water reduction.

1. Introduction

Hydrogen, a clean and free-carbon energy, deserves special attention for the increasing energy crisis. Converting water into fuel is verified to be a friendship strategy, since it has the advantages to generate fuels even reduce greenhouse gases [1,2]. Photocatalytic water splitting to hydrogen via using semiconductors, obviously, has been adjudged a promising and sustainable method [3,4]. Particularly, cuprous oxide (Cu$_2$O) with a direct band gap of 2.0 eV and favorable energy band positions [5–7], is identified as one of the most promising photocathodes for water reduction by solar among the investigated materials [8–11]. Furthermore, Cu$_2$O is abundant, non-toxic, low-cost, and eco-friendly [12–14]. Unfortunately, rapid recombination of photogenerated electron-hole pairs [15,16] and deficient active sites for proton reduction [17,18] resulted in poor activity of bare Cu$_2$O towards for photocatalytic hydrogen evolution reaction (HER). Therefore, to improve the separation of photogenerated electron-hole pairs and the capability of photocatalytic HER, integration of cocatalyst on Cu$_2$O nanocrystals has been confirmed to be one of the most effective methods.

In the history of cocatalysts, noble metals (like Pt, Au, Ag) have been noted firstly to modify the photocatalytic activities of semiconductors [15,19–21], but soaring cost and scarce restricted their widespread use. Exploring abundance and inexpensive cocatalysts is urgent, hence, transitional metal compounds [22–24] are developed. Typically, transition metal sulfides act as cocatalysts have been received extensive attention as their excellent performances, such as MoS$_2$ [25,26], WS$_2$ [27,28], PtS [29], NiS [30], and CoS [31] et al., both of the chalcogenides cocatalysts mainly serve as adsorption sites for hydrogen atoms and finally enhance the photocatalytic performances. However, for the cocatalyst of copper chalcogenide (e.g. Cu$_7$S$_4$), which exhibits localized surface plasmon resonances (LSPR) character as the presence of plentiful Cu vacancies, and shows absorption ability in the near-infrared (NIR) region [32,33], meanwhile provides active sites, thus the improved photocatalytic properties mainly come from LSPR feature and active sites. For example, the Cu$_7$S$_4$@Pd nanocrystals with excellent NIR LSPR properties and photocatalytic activities towards for degradation organics were synthesized

by Cui et al. [32], and the results manifested that the Cu_7S_4 phase serves as a plasmonic component for efficient photo-harvesting in NIR region. Other photocatalytic applications of Cu_7S_4 were also revealed, but principally focused on the degradation organics [34,35], photothermal [36], bactericidal [37], and light-induced water evaporation [38]. Moreover, the literatures for Cu_7S_4 nanocrystals applied to photocatalytic HER just acts as semiconductors [39] or templates [40] rather than acts as cocatalysts to data. Consequently, we wonder if Cu_7S_4 phase formed on the surface of host photocatalysts as a cocatalyst, and whether the resultant photocatalysts can enhance the photocatalytic activities of the host photocatalysts.

Therefore, Cu_7S_4 serves as cocatalyst and is formed on Cu_2O nanocubes in situ, the obtained Cu_2O/Cu_7S_4 NCs are firstly employed to photocatalytic HER. The optimally obtained Cu_2O/Cu_7S_4 NCs show obviously enhanced light harvesting, activity and stability for photocatalytic HER in neutral solution under full spectra illumination, and the hydrogen production rate can reach to 1689.00 $\mu mol\, g^{-1}\, h^{-1}$ at ambient temperature. The improved photocatalytic performance is mainly ascribed to that the LSPR of Cu_7S_4 can significantly suppress electron-hole pairs recombination, remarkably enhance conductivity, promote electron transfer, increase the light absorption, and the Cu_7S_4 layers also provide active sites for proton reduction, thus the photocatalytic activity for HER is enhanced.

2. Experimental procedures

2.1. Reagents and materials

Copper (II) chloride dihydrate ($CuCl_2\cdot 2H_2O$, 99.0%), sodium sulphate anhydrous (Na_2SO_4, ≥99%), and L-ascorbic acid (l-AA, 99.7%) were purchased from Sinopharm Chemical Reagent Co., Ltd. Sodium sulfide nonahydrate ($Na_2S\cdot 9H_2O$, 99.0%) was purchased from Adamas Reagent Co., Ltd. Ethanol (CH_3CH_2OH, ≥99.8%), ethylene glycol ($HOCH_2CH_2OH$, ≥99.5%), and isopropyl alcohol (C_3H_8O, ≥99.8%) were purchased from Kermel (Tianjin, China). Sodium sulphate anhydrous (Na_2SO_3, ≥97%) was purchased from Tianjin Fuyu Fine Chemical Co., Ltd. Deionized (DI) water was used in the entire experiments. All chemicals were used as received without further purification. Fluorine-doped tin oxide (FTO) conductively glass (14 $\Omega\, cm^{-2}$, Nippon Sheet Glass, Wuhan) was cleaned with acetone, alcohol and deionized water for 30 min, respectively.
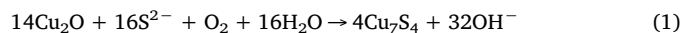
2.2. Preparation of cube Cu_2O nanocrystals

Cube Cu_2O nanocrystals were synthesized through a modified simple solution method [41]. In detail, 0.1 M 2.5 mL $CuCl_2\cdot 2H_2O$ solution and 0.2 M 7.5 mL NaOH solution were sequentially introduced into a 250 mL screw mouth glass bottle with 100 mL DI water. The precursor was stirred at room temperature with a speed of 300 rpm for 5 min until a homogeneous light-blue solution formed. 0.1 M 5 mL L-AA solution was then injected and maintained for 30 min at ambient temperature. The mixture color from light blue to limpid orange was observed, indicating the coordination between the methine of L-AA and Cu^{2+} cations. Afterwards, the nanocrystals were isolated by centrifugation at 15,000 rpm for 5 min, then sonicated and washed thrice by redispersion with DI water and alcohol. Finally, the nanocrystals were freeze-dried and preserved.

2.3. Fabrication of Cu_2O/Cu_7S_4 NCs in situ

Cu_7S_4-coated Cu_2O nanocubes (NCs) were generated in situ by the anion exchange method [42], and varying degree of cure can be precisely controlled by adding different Moore ratios of $Na_2S\cdot 9H_2O$ to Cu_2O. Typically, 8.68 mg Cu_2O dispersed in a 40 mL beaker with 25 mL DI water was sonication for 30 min to form a homogeneous solution. Various Moore weight of 0.1 M $Na_2S\cdot 9H_2O$ were then injected after the

beaker was placed in ice water of 5 °C for 5 min, and continuously stirred with a speed of 300 rpm and kept for 15 min. Cu_2O on the NCs surface would be converted into Cu_7S_4 thin layers immediately when suspended in the Na_2S solution as Cu_7S_4 with much smaller solubility product constant ($K_{sp} \approx 10^{-48}$) than that of Cu_2O (Eq. (1)) [43].

$$14Cu_2O + 16S^{2-} + O_2 + 16H_2O \rightarrow 4Cu_7S_4 + 32OH^- \qquad (1)$$

The nanocrystals were isolated by centrifugation at 15,000 rpm for 5 min, then sonicated and washed thrice by redispersion with ethanol and DI water. Finally, the nanocrystals were freeze-dried and preserved. The obtained nanocrystals were named as S-x/Cu_2O, x in which represented the Moore ratio of $Na_2S\cdot 9H_2O$ to Cu_2O. For example, x = 1 stood for the Moore ratio is 1, and the addition volume of $Na_2S\cdot 9H_2O$ is 60 μL, and the other specimens (such as, x = 2, 3, 4, 5, 6, 8, 10, 12, 20) were synthesized in a similar fashion. According to the transient photocurrents of various cure degree (Fig. S1), the S-3/Cu_2O sample with the highest transient photocurrent and was selected to investigate the effect of trace sulfuration on the photocatalytic properties of Cu_2O, and Cu_2O/Cu_7S_4 NCs represented S-3/Cu_2O in the next context without specified explanation. Moreover, the sample just only was Cu_7S_4 phase as the Moore ratio of 20:10, and termed as Cu_7S_4 NCs, which can be verified by XRD pattern in Fig. S2.

2.4. Materials characterizations

Powder X-ray Diffraction (XRD) patterns were recorded by using a Brooker D8 advanced X-ray diffractometer with Cu-Kα radiation (λ = 1.5418 Å). Scanning electron microscopy (SEM) images were taken on a JSM-7800F thermal field scanning electron microscope operated at 15 kV. Transmission electron microscopy (TEM), high-resolution TEM (HRTEM) images, energy-dispersive X-ray spectroscopy (EDS) line scan and mapping analyses were conducted on a JEOL 2100F field-emission high-resolution transmission electron microscope operated at 200 kV.

UV-VIS-NIR spectra were tested in the spectral region of 300–2000 nm with a Lambda 750 spectrophotometer (Perkin Elmer), and the bandgaps of samples were determined from the Tauc Plots with the wavelength from 300 nm to 800 nm. Defects in semiconductors can be confirmed by Fluorescence (RF-5301PC, Perkin Elmer). The surface composition, electronic structure and valence-band spectra of the specimens were characterized by X-ray photoelectron spectroscopy (XPS, Kratos AXIS Ultra DLD). And all the spectra were calibrated to the C 1s peak at 284.6 eV.

2.5. Photocatalytic hydrogen production testing

The photocatalytic water reduction was conducted in a homemade 150 mL sealed quartz glass cell with 100 mL 0.5 M Na_2SO_3 as sacrificial agent. Then, 10 mg photocatalyst with dry powder dissolved and sonicated in an argon flow for 30 min to eliminate oxygen. The light irradiation was a 300-W Xe lamp (Solaredge 700, China) with the full spectra, and the light power density was 100 $mW\, cm^{-2}$. Hydrogen evolution amount was measured via gas chromatography (GC-2014, SHIMADZU) and performed for 4 h. The photostability of Cu_2O/Cu_7S_4 NCs was estimated every 4 h and the test was repeated for 5 cycles.

2.6. Photoelectrochemical measurements

5.0 mg of nanocrystals were dispersed in isopropyl alcohol and ethylene glycol mixed of 250 μL with the volume is 1:1, the slurry then uniformly dropped onto a 1 × 1.5 cm^2 FTO glass to cover the area of 1 × 1 cm^2. The FTO glass was then dried in a drying oven at 60 °C for 12 h. A standard three-electrode setup was used, the FTO glass coated with samples as working electrode (as shown in Fig. S3), a carbon rod as counter electrode, and Ag/AgCl electrode as reference electrode. The

three electrodes were inserted in a quartz cell filled with 0.5 M Na$_2$SO$_4$ electrolyte for photoelectrochemical measurements. Prior to testing, the electrolyte was purged with Ar for 30 min to removal the oxygen. A 300-W Xe lamp (Solaredge 700, China) with AM 1.5G simulated sunlight as light source, and the power density of light was tested to be 100 mW cm^{-2} for full spectrum.

The transient photocurrent was measured on a CHI 660D electrochemical station (Shanghai Chenhua, China) in ambient conditions under chopped light irradiation (light on/off cycles are 10 s) at a 0 V bias potential (vs. reversible hydrogen electrode (RHE)) for 240 s, with a scan rate of 10 mV s^{-1}. The stability tests of samples were conducted for 2 h. Linear sweep voltammetry (LSV) curves for Cu$_2$O and Cu$_2$O/Cu$_7$S$_4$ NCs were measured with a scan rate of 10 mV s^{-1}, and the potential ranged from 0 V to 0.6 V (vs. RHE). Electrochemical impedance spectroscopy (EIS) was conducted by using a potentiostat (CHI 660D) with the amplitude of 10 mV and a frequency from 0.01 kHz to 100 kHz. The Mott-Schottky (M–S) plots were obtained at a constant frequency of 1.0 kHz, and the electrolyte was 0.5 M Na$_2$SO$_4$ aqueous solution.

The measured E_{FB} value can be converted to the normal hydrogen electrode (NHE) scale via the Nernst equation (Eq. (2)) [44]:

$$E_{NHE} = E_{Ag/AgCl} + E°_{Ag/AgCl} \qquad (2)$$

Where E_{NHE} is the converted potential vs NHE, $E_{Ag/AgCl}$ the experimental potential measured against the Ag/AgCl reference electrode, and $E°_{Ag/AgCl}$ the standard potential of Ag/AgCl at 298 K (0.197 V).

The solar energy conversion efficiency was calculated via Eq. (3) [45] showed as follows:

$$\text{solar energy conversion efficiency} = ((|J| \times [V_{RHE} - V_{H+/H2}])/p) \times 100\% \qquad (3)$$

Where V_{RHE} is the applied potential versus RHE, $V_{H+/H2}$ is the Nernst potential for H$_2$ evolution (0 V vs RHE), J is the photocurrent (mA cm^{-2}) under AM 1.5G irradiation, and P is the incident solar irradiance (100 mW cm^{-2} for AM 1.5G).

3. Results and discussion

3.1. Morphology, nanostructure, and composition of hybrid catalysts

The optimal Cu$_7$S$_4$-coated Cu$_2$O NCs are obtained after comparing the transient photocurrents (see detail in Fig. S1), and which is donated as Cu$_2$O/Cu$_7$S$_4$ NCs in the next. The morphology, adhesion state, size and uniformity can be detected by SEM as shown in Fig. S4, which indicates the cubic morphology, strongly integration and the average size of Cu$_2$O and Cu$_2$O/Cu$_7$S$_4$ NCs are 47.28 nm and 58.27 nm, respectively. Several voids are appeared in Cu$_2$O/Cu$_7$S$_4$ NCs (Fig. S4b), due to the fact that the Kirkendall effect induced net directional flow of materials at the template/reactant interfaces [43], and accompanied by the increasing of particle diameter (Fig. S4).

The TEM morphology of Cu$_2$O/Cu$_7$S$_4$ NCs (Fig. 1a) and bare Cu$_2$O NCs (Fig. S4a) are further revealed the cube structure. Moreover, the Cu$_2$O/Cu$_7$S$_4$ NCs represent a core-shell structure with a clearly heterogeneous interface (Fig. 1a). The HRTEM image in Fig. 1b displays a shrunken interplanar spacing of 0.2108 nm, which is corresponding to the (200) plane of Cu$_2$O NCs with a well crystallized structure, as compared to the pure Cu$_2$O NCs (shown in Fig. S5b with an interplanar spacing of 0.2130 nm). Furthermore, typical lattice fringes with an interplane spacing of 0.1948 nm is also detected in Fig. 1b, which is a powerful evidence for the presence of roxbyite Cu$_7$S$_4$ with (0160) lattice plane. Hence, the Cu$_2$O/Cu$_7$S$_4$ NCs in Fig. 1b with two sets of lattice planes can be revealed the integration of Cu$_2$O and Cu$_7$S$_4$ NCs. Each element amount is described in Fig. S6, which can certify the presence of sulfur in Cu$_2$O/Cu$_7$S$_4$ NCs. To further confirm that the elements are Cu, O, and S and their distribution in Cu$_2$O/Cu$_7$S$_4$ NCs, EDS line scan and mapping analyses were conducted (Fig. 1c and d). Obviously, S

element is chiefly uniformly distributed in the outer shells, and O element is primarily distributed in inner, whereas, Cu element is evenly distributed in the overall NCs. Above all, it can be induced that highly integration Cu$_2$O/Cu$_7$S$_4$ NCs are successfully prepared.

For further determining the phase in Cu$_2$O and Cu$_2$O/Cu$_7$S$_4$ NCs, typical XRD patterns are recorded in Fig. 2a. It demonstrates that the peaks are all assigned to cuprite Cu$_2$O (Pn-3m) with a strong (111) orientation (PDF No. 05-0667) in Cu$_2$O NCs, and no peaks of CuO is identified. A clearly peak of (0160) lattice plane for roxbyite Cu$_7$S$_4$ (C2/m) (PDF No. 23-0958) can be observed in Cu$_2$O/Cu$_7$S$_4$ NCs. Thus, it can be concluded that Cu$_7$S$_4$ phase is formed on the surface of Cu$_2$O induced by anion exchange and forming a core-shell structure (Fig. 1a). The range of 35–43° (2θ) in XRD patterns are enlarged and displayed in Fig. S7, a distinct shift is obtained for Cu$_2$O (111) and (200) of ca. 0.006° and 0.101°, respectively. The degree shifts to higher angle may be ascribed to the presence of Cu$_7$S$_4$ layers, and which is agreement with the results attained in HRTEM (Fig. 1b and Fig. S5b). Consequently, a unique and uniform coverage of Cu$_7$S$_4$ on Cu$_2$O surface by Kendall effect is acquired, which is demonstrated with the mapping (Fig. 1d) and XRD results (Fig. 2a).

XPS survey spectra for Cu$_2$O and Cu$_2$O/Cu$_7$S$_4$ NCs are depicted in Fig. S8 to confirm the surface composition, and elemental sulfur is detected in Cu$_2$O/Cu$_7$S$_4$ NCs. The full spectrum of Cu$_2$O is displayed in Fig. S8a, which shows that the binding energy of O 1s at 532 eV and Cu 2p at 933 eV. For Cu$_2$O/Cu$_7$S$_4$ NCs (Fig. S8b), S 2p peak at 163 eV is detected as sulfuration, accompanied by the O 1s and Cu 2p peaks. However, the intensity of O 1s peak decreasing with sulfuration, implying that a certain degree of Cu$_2$O reduction. High resolution XPS spectra of Cu 2p, O 1s, and S 2p are described in Fig. 2b, c, and d, respectively, to further verify the chemical states of each element. In Fig. 2b, Cu 2p core level XPS spectra of Cu$_2$O/Cu$_7$S$_4$ and Cu$_2$O NCs show that Cu(I) 2p$_{3/2}$ and Cu(I) 2p$_{1/2}$ spin-orbital components with high binding energy peaks, which locate at 931.81 eV (931.28 eV for Cu$_2$O) and 951.59 eV (951.71 eV for Cu$_2$O), respectively [46]. Moreover, Cu$^+$ is the main surface species is indicated instead of zero valence Cu, which is consistent with the Cu LMM Auger peak at 916.98 eV (916.78 eV for Cu$_2$O) of Cu(I) 2p$_{3/2}$ and 917.15 eV (917.45 eV for Cu$_2$O) of Cu(I) 2p$_{1/2}$ in Fig. S9. A slight negative shift of Cu(I) 2p$_{3/2}$ is observed, it can be induced that S−Cu(I)−O bonds displace Cu(I)−O bonds [47]. Obviously, a series of shakeup satellite peaks with higher binding energies are also detected in Cu$_2$O/Cu$_7$S$_4$ and Cu$_2$O NCs, which donating that the presence of Cu(II) oxide [48]. Furthermore, the intensity of Cu(II) peaks in Cu$_2$O/Cu$_7$S$_4$ NCs surpass that in Cu$_2$O, and may be attributed to the amorphous character of CuO layer [47] which is undetected in the HRTEM image (Fig. 1b) and XRD patterns (Fig. 2a).

From the O 1s core level spectra of Cu$_2$O/Cu$_7$S$_4$ and Cu$_2$O in Fig. 2c, the O 1s peak at 531.25 eV of Cu$_2$O/Cu$_7$S$_4$ NCs with negative shift relative to that of Cu$_2$O lies at 531.40 eV, and which can be resulted from the presence of sulfur in the Cu$_2$O lattice [48], and further supporting the S−Cu(I)−O bonds formation. Otherwise, the binding energy of 529.87 eV for O 1s in Cu$_2$O NCs displays the lattice oxygen [49], while this peak disappears in Cu$_2$O/Cu$_7$S$_4$ NCs, which also indicates the formation of S−Cu(I)−O bonds. Chemical state of S atoms in Cu$_2$O/Cu$_7$S$_4$ NCs is explicated via analyzing the S 2p core levels spectrum in Fig. 2d, binding energy of S 2p$_{3/2}$ and 2p$_{1/2}$ lie at 161.85 eV and 163.15 eV, respectively, and manifesting the metal sulfides generation [50]. In addition, a binding energy of 168.65 eV is also observed in Fig. 2d, which can be assigned to the presence of SO$_4^{2-}$ functional group on Cu$_2$O/Cu$_7$S$_4$ NCs surface [51]. In result, the oxygen atoms on Cu$_2$O surface have been partially replaced by sulfur atoms, which can be induced from the results of HRTEM (Fig. 1b), XRD (Fig. 2a), and XPS (Fig. 2c–d), and thus the Cu$_2$O/Cu$_7$S$_4$ NCs photocathode catalyst is successfully prepared.
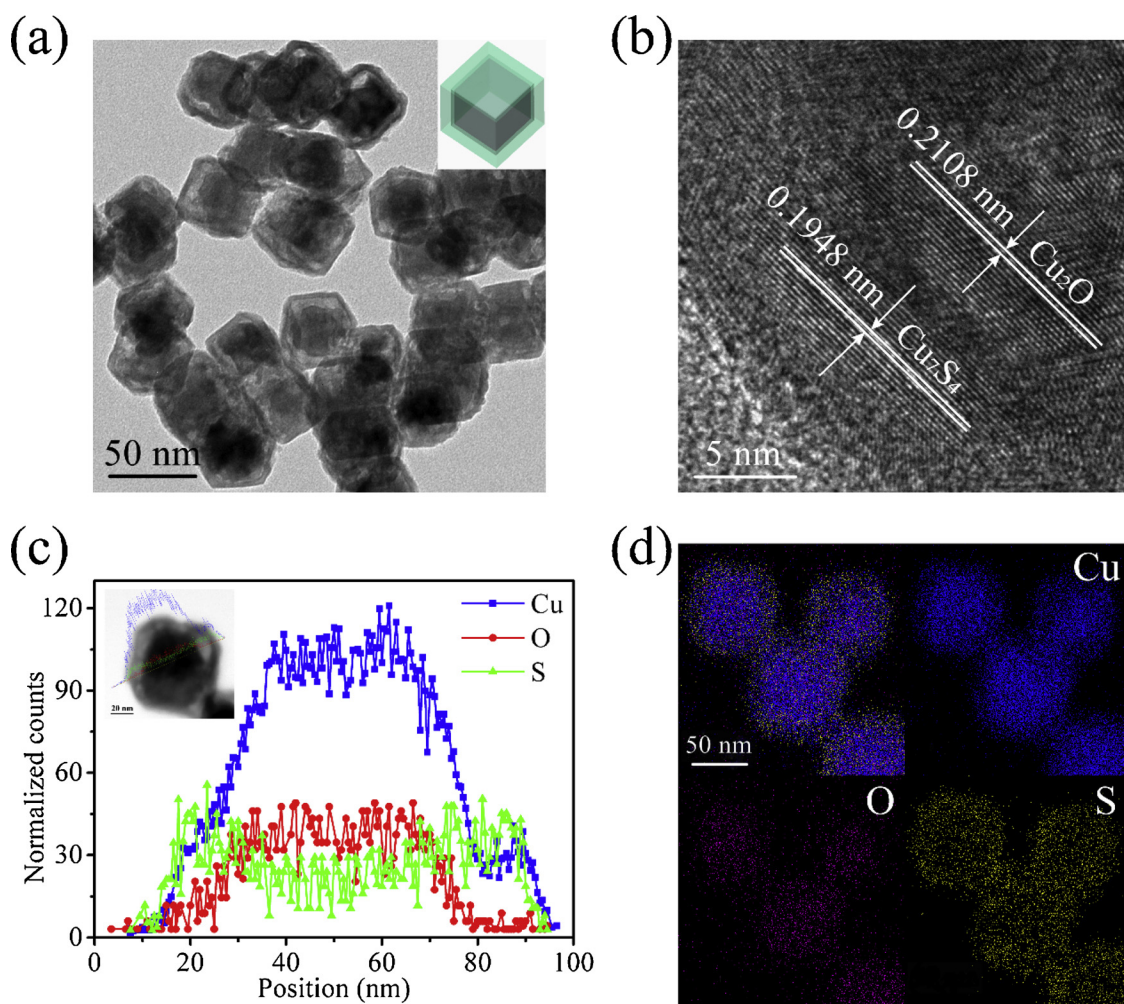
Fig. 1. High-resolution transmission electron microscopy of the Cu_2O/Cu_7S_4 NCs sample obtained after anion exchange. (a) TEM image (insert is the structure of the specimen), (b) HRTEM image, (c) STEM image and EDS line scan profiles, and (d) EDS mapping profiles.

3.2. Photocatalytic activity for HER

UV-VIS-NIR absorption spectra were employed to study the light absorption and the photocatalytic capacity of Cu_2O/Cu_7S_4 and Cu_2O NCs, as reflected in Fig. 3a. In the visible region, a broad spectrum of harvesting solar lights can be offered by the Cu_2O/Cu_7S_4 NCs (absorbance edge reaches to 635 nm of Cu_2O/Cu_7S_4 NCs, which broader than that of Cu_2O is 608 nm). Moreover, a peak for NIR absorption can be observed at 1500 nm in Fig. 3a, which indicates the presence of NIR absorption in Cu_2O/Cu_7S_4 NCs sample. The Tauc plots in Fig. 3b can be calculated from the absorption spectra (with the wavelength ranges from 300 nm to 800 nm) in Fig. 3a, and the bandgap energy are 2.04 eV and 1.96 eV for Cu_2O and Cu_2O/Cu_7S_4 NCs, respectively. Bandgap energy with small shrunk is observed in Cu_2O/Cu_7S_4 NCs compared to Cu_2O NCs, which is due to the large absorbance edge as seen in Fig. 3a. Thus, the enhanced light absorption and shrunk bandgap energy both can be estimated that the presence of Cu_7S_4 layer facilitate to the photocatalytic activity.

To contrast the photocatalytic H_2 production quantitatively in Cu_2O, Cu_7S_4 and Cu_2O/Cu_7S_4 NCs, which can be assessed by the GC. Cu_2O, Cu_7S_4 and Cu_2O/Cu_7S_4 NCs were readily dispersed in DI water, and the photoexcited holes were quenched with 0.5 M Na_2SO_3 sacrificial solution. From Fig. 3c, negligible hydrogen production rate of Cu_7S_4 NCs (126.16 $\mu mol g^{-1} h^{-1}$) is received under full spectra irradiation, and revealing that in the photocatalyst of Cu_2O/Cu_7S_4 NCs, Cu_7S_4 basically acts as cocatalyst. The Cu_2O/Cu_7S_4 NCs with higher H_2

production rate of 1689.00 $\mu mol g^{-1} h^{-1}$ than that of Cu_2O is 986.75 $\mu mol g^{-1} h^{-1}$ under the full spectra illumination, which is also demonstrated in Fig. 3c, meanwhile testify the function of Cu_7S_4 in photocatalysis. In addition, the photostability of Cu_2O/Cu_7S_4 NCs was evacuated every 4 h and the durability test was repeated for 5 times. As can be seen from Fig. 3d, the photocatalytic stability of Cu_2O/Cu_7S_4 NCs is only little decline ($\leq 6\%$) in HER via solar after the fifth cycle. Moreover, the hydrogen production can be comparable with other photocatalysts reported by references and list in Table S1. According to Table S1, the highest hydrogen production rate is obtained in this work, in part because the used sacrificial regent is facilitated to the dissociation of water. For the sacrificial regent of Na_2SO_3, which was dissolved in water and oxidized by photogenerated holes, then formed HSO_4^- (Eq. (4)) and ionization (Eq. (5)):

$$SO_3^{2-} + H_2O \rightarrow HSO_4^- + H^+ \tag{4}$$

$$HSO_4^- \rightarrow SO_4^{2-} + H^+ \tag{5}$$

Reduction of H^+ in aqueous solution containing the tested photocatalysts can be displayed in Eq. (6) to produce hydrogen.

$$H^+ + e^- \rightarrow H_2 \tag{6}$$

3.3. The reasons for enhancing photocatalytic property

To reveal the origins of the apparently improved photocatalytic

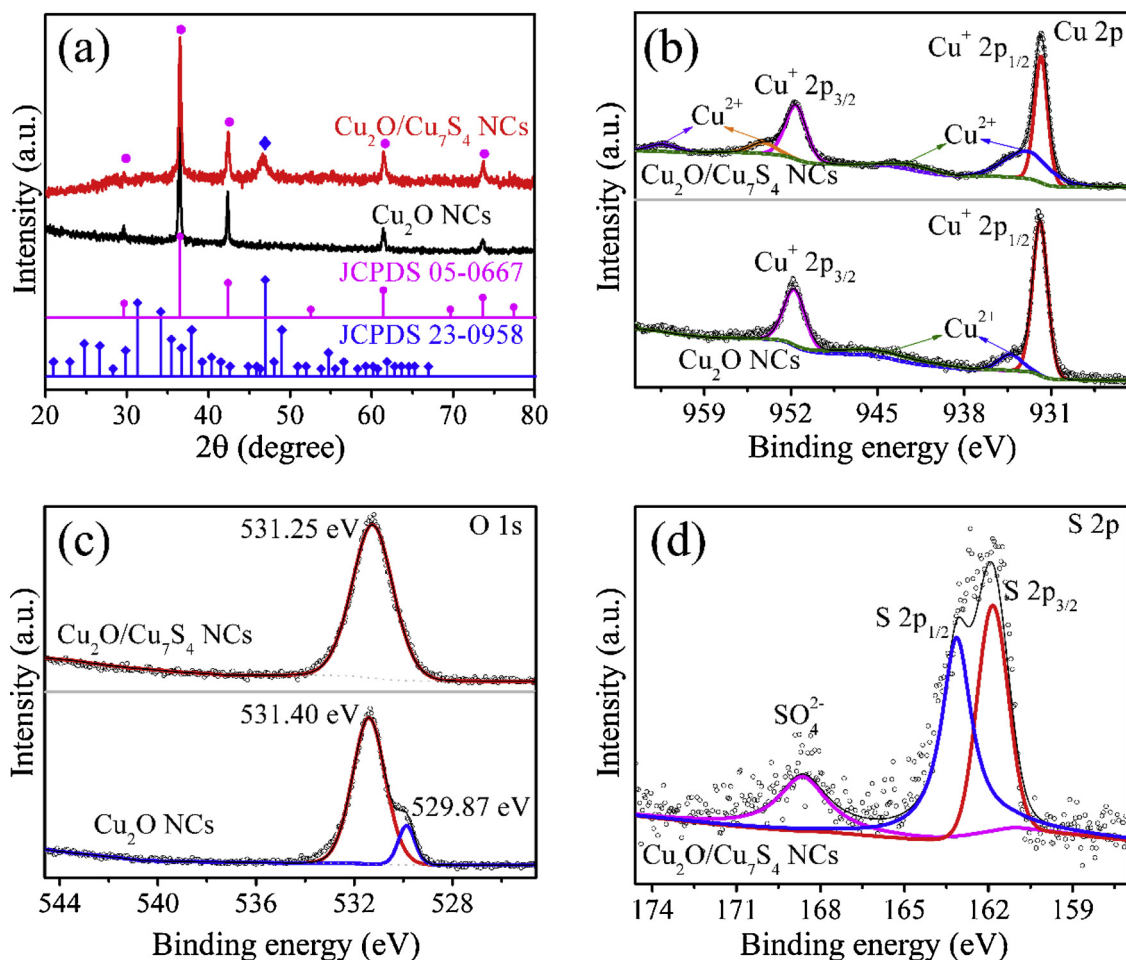**Fig. 2.** (a) Powder XRD patterns of i) standard Cu_2O (JCPDS file 05-0667), ii) the Cu_2O/Cu_7S_4 NCs, iii) standard Cu_7S_4 (JCPDS file 23-0958). High resolution XPS spectra of (b) Cu 2p, (c) O 1s, (d) S 2p for Cu_2O and Cu_2O/Cu_7S_4 NCs.

hydrogen evolution for the Cu_2O/Cu_7S_4 NCs photocatalyst, a series of characterizations are conducted in both Cu_2O and Cu_2O/Cu_7S_4 NCs samples. By means of consulting literatures [30,52,53], photoelectrochemical properties are deemed to be a valid proof for confirming the separation of photogenerated electron-hole pairs and the transfer of carriers, for instance, EIS, I–V, Mott-Schottky plots, and transient photocurrent. An increased current density is observed in the polarization curves of Fig. 4a as compared Cu_2O/Cu_7S_4 NCs with Cu_2O NCs, implying that the photocatalytic activity towards for HER is promoted via the Cu_7S_4 cocatalyst. It may be due to that the Cu_7S_4 cocatalyst with superior conductivity and LSPR character [32]. Meanwhile, a high converted solar efficiency in Cu_2O/Cu_7S_4 NCs instead of that in Cu_2O NCs is showed in Fig. S10. Transient photocurrent density of Cu_2O and Cu_2O/Cu_7S_4 NCs under full spectrum illumination with 10 s light-off cycles is showed in Fig. 4b. Obviously, the photocurrent of Cu_2O/Cu_7S_4 NCs is superior to that of Cu_2O NCs, furthermore, almost no spikes in Cu_2O/Cu_7S_4 NCs (Fig. 4b) while a distinct spike is generated in Cu_2O NCs (Fig. S11), suggesting that the cocatalyst Cu_7S_4 layers formed on the surface of Cu_2O/Cu_7S_4 NCs in situ is beneficial to separate the photogenerated electron-hole pairs. More stable operation of Cu_2O/Cu_7S_4 NCs than that of Cu_2O NCs is observed in Fig. S12, which are measured in a PEC cell (Fig. S13), and the photostability for Cu_2O NCs is only of 66.47%, while the photostability of Cu_2O/Cu_7S_4 NCs increases to 74.74%. In brief, photogenerated electrons and holes recombination can be hindered with a certain mass of Cu_7S_4 produced on Cu_2O NCs surface (Fig. 4b), thus facilitating electron transfer fast and raising photostability in Cu_2O NCs (Fig. S12).

For determining the carrier concentrations and flat-band potentials

(E_{Fb}) of Cu_2O and Cu_2O/Cu_7S_4 NCs, M–S tests were conducted, and the results are depicted in Fig. 4c. Negative slopes are derived from the M–S plots (Fig. 4c), confirming the p-type semiconductors character with hole conduction. Furthering, the donor concentrations in Cu_2O and Cu_2O/Cu_7S_4 NCs can be quantified by the Mott-Schottky equation [54] (Eq. (7)).

$$1/C^2 = (2/(e\varepsilon\varepsilon_0 N_D))[(V - V_F) - kT/e] \tag{7}$$

Where C represents capacitance in space charge region, e is electron charge, ε_0 means vacuum permittivity ($\varepsilon_0 = 8.85 \times 10^{-14}\,F\,cm^{-1}$), ε is dielectric constant of material (for Cu_2O, $\varepsilon = 6.3$ [55]), V is electrode applied potential, k is Boltzmann constant, N_D means carrier concentration. And the donor concentrations are then estimated from the M–S plot slops by using Eq. (8) [54]

$$N_D = (2/(e\varepsilon\varepsilon_0))[d(1/C^2)/dV]^{-1} \tag{8}$$

For Cu_2O and Cu_2O/Cu_7S_4 NCs, thus, the hole concentrations are calculated to be $1.44 \times 10^{20}\,cm^{-3}$ and $3.7 \times 10^{20}\,cm^{-3}$, respectively, which is comparable to the typical values in references [54,55]. Besides, the Cu_2O/Cu_7S_4 NCs nearly 2.57 times hole concentration of Cu_2O NCs, which implies that the presence of Cu_7S_4 can accelerate electron transfer. In addition, the E_{Fb} of 1.314 and 1.291 V (vs. NHE) for Cu_2O and Cu_2O/Cu_7S_4 NCs are also obtained from Fig. 4c, respectively.

In addition, EIS measurement was employed to investigate the electrical transport properties of Cu_2O and Cu_2O/Cu_7S_4 NCs. EIS arc radii in Fig. 4d display that a smaller semicircle of Cu_2O/Cu_7S_4 NCs than that of Cu_2O NCs, manifesting that the resistance of electron transfer via the interface layer in Cu_2O/Cu_7S_4 NCs is reduced. The
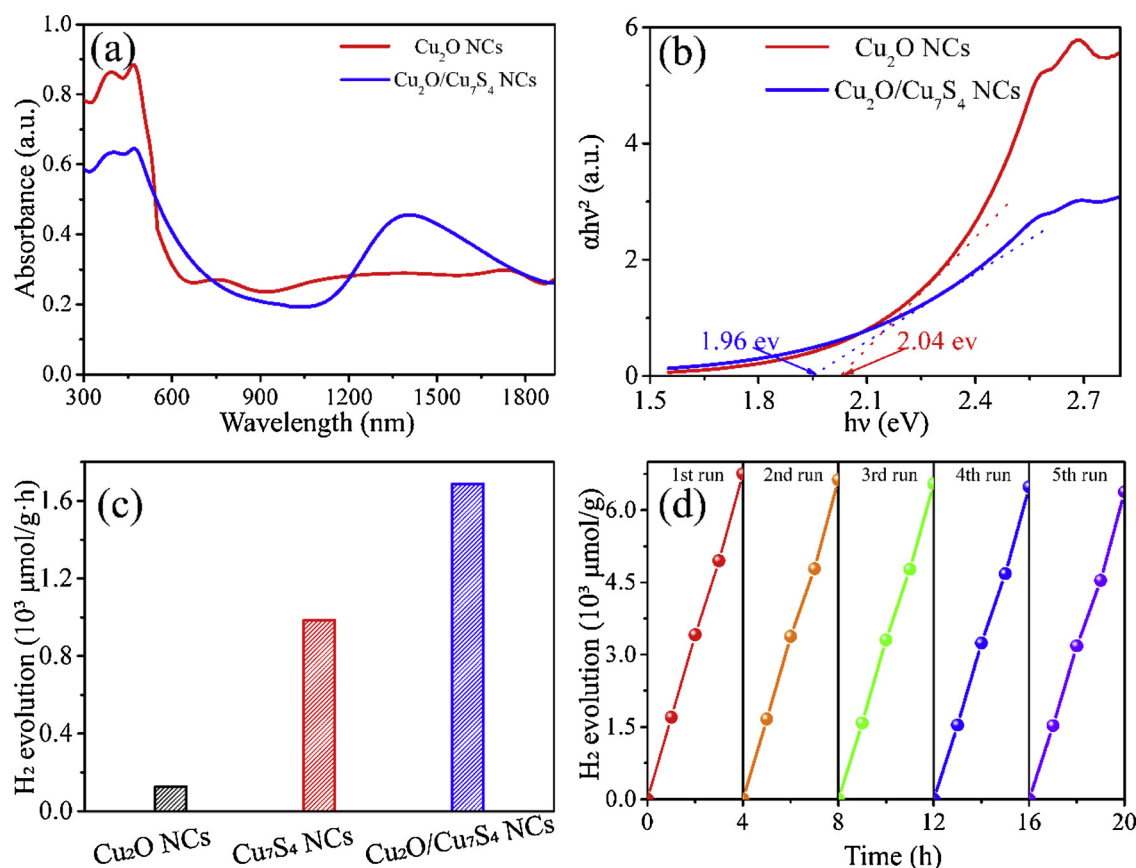
Fig. 3. (a) UV-VIS-NIR absorption for the pure Cu_2O and Cu_2O/Cu_7S_4 NCs. (b) The relationship between $(\alpha h\nu)^2$ and $h\nu$ of pure Cu_2O and Cu_2O/Cu_7S_4 NCs, which is calculated from Fig. 3a and the wavelength ranges from 300 nm to 800 nm. (c) Photocatalytic hydrogen production rate of Cu_2O, Cu_7S_4 and Cu_2O/Cu_7S_4 NCs. (d) The photostability of Cu_2O/Cu_7S_4 NCs under full spectra irradiation.

results certified again the effective interfacial electron-hole pairs separation and carriers transfer in the Cu_2O/Cu_7S_4 NCs. In general, the Cu_7S_4 layers facilitate electron transfer from Cu_2O to electrolyte, resulting in an overall decreasing charge transfer resistance (Fig. 4d), and which are also consistent with the LSV (Fig. 4a) and photoresponse (Fig. 4b) results.

To further interpretation the charge transfer velocity, the PL spectra are presented in Fig. 5a, 460 nm wavelength as excitation spectra for Cu_2O and Cu_2O/Cu_7S_4 NCs. Lower characteristic peak intensity in Cu_2O/Cu_7S_4 NCs is observed than that in Cu_2O NCs, indicating that the photogenerated electron-hole pairs recombination rate has been markedly alleviated, and this finding is consistent with the result in Fig. 4b. Besides, the reduced PL intensity in Cu_2O/Cu_7S_4 NCs also confirms that the efficiency of interfacial electron transfer from photoexcited Cu_2O to Cu_7S_4.

Furthermore, $Cu_{2-x}S$ with LSPR and LSPR intensity is heavily relies on free carrier density in the form of cation deficiencies has been reported [33]. To clarify the possible involvement of Cu_7S_4 LSPR in Cu_2O/Cu_7S_4 NCs, LSPR absorption spectra is estimated from 600 nm to 2000 nm, compared to Cu_2O NCs as shown in Fig. 5b. Cu_2O NCs displays a LSPR peak only at ca. 750 nm, while the peak intensity at 750 nm is enhanced and another broad absorption spectrum (ca. 1500 nm) is also observed in Cu_2O/Cu_7S_4 NCs. Therefore, the enhanced LSPR absorption at 750 nm and extra LSPR peak emerged at ca. 1500 nm [32] can be ascribed to the presence of Cu_7S_4 with Cu vacancies. Moreover, LSPR effect is relative to local electrical field enhancement [32], and strong LSPR with strong local electrical field, suggesting a promising way to effectively enhance the local electrical field by introducing Cu_7S_4. Furthermore, electron transfer velocity can be increased by the improved local electrical field resulted from the

LSPR of Cu_7S_4.

To reveal the energy band structures of samples, the XPS valence band spectra (Fig. 6a), Mott–Schottky plots (Fig. 4c), and bandgap energy (Fig. 3b) are conducted. Fig. 6a indicates that the VB edges of Cu_2O and Cu_2O/Cu_7S_4 NCs are located at 1.819 eV and 1.664 eV, respectively. Combining the results from Figs. 3b, 4c and 6a, the energy level diagrams of Cu_2O and Cu_2O/Cu_7S_4 NCs can be deduced (Fig. 6b). As the band alignment shown in Fig. 6b, the bandgap in Cu_2O and Cu_2O/Cu_7S_4 NCs are both large enough (≥ 1.6 eV) to split water, meanwhile, small enough (≤ 2.2 eV) to harvest much light in a wide range [56]. However, reduced bandgap and more negative of CB relative to HER potential can be attained in Cu_2O/Cu_7S_4 NCs, so large driving force for water reduction can be gained and accompanied by the absorption edge increasing. Moreover, it can be seen that the E_{Fb} of Cu_2O/Cu_7S_4 NCs with much smaller difference value with the normal hydrogen and oxygen evolution potential, meaning the remained electrons decreased, and further displays that more electrons are transferred from Cu_2O/Cu_7S_4 NCs surface to electrolyte.

Therefore, based on the above data and analysis, the possible mechanism is proposed and illustrated in Fig. 7. Firstly, interfacial charge equilibrium is established between Cu_2O and Cu_7S_4 interaction in Cu_2O/Cu_7S_4 NCs. Electrons in the VB can be excited to the CB with holes simultaneously generating in VB, as the simulated solar light with enough photon energy. Under light illumination, some of photogenerated electrons, which are distributed at the interfaces of Cu_2O and Cu_7S_4, transfer into the Cu_7S_4 layers until new interfacial charge equilibrium is reached. Thus, the adsorbed H^+ to H_2 reduced on Cu_7S_4 surfaces as the photogenerated electrons from Cu_2O transfer to Cu_7S_4, the left holes in Cu_2O would have much lifetime to carry out the oxidation of SO_3^{2-} to SO_4^{2-} in photocatalysis (four electrons process of
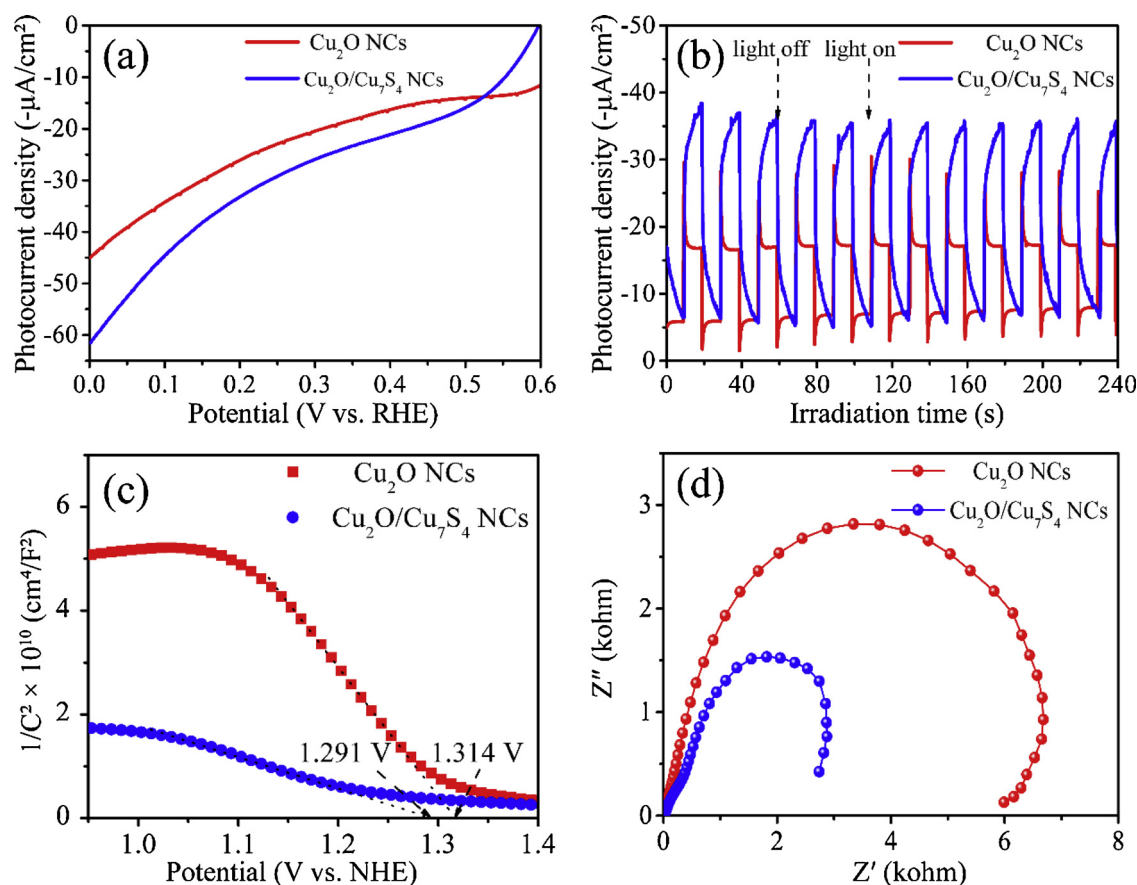
Fig. 4. Photoelectrochemical measurements for Cu_2O and Cu_2O/Cu_7S_4 NCs in 0.5 M Na_2SO_4: (a) Linear sweep voltammetry curves at the potential from 0.6 V to 0.0 V vs RHE. (b) Photocurrent vs. time (I–t) curves with the light-off is 10 s. The power density of full-spectrum irradiation is 100 mW cm^{-2}. (c) Mott-Schottky plots. (d) Electrochemical impedance spectra.
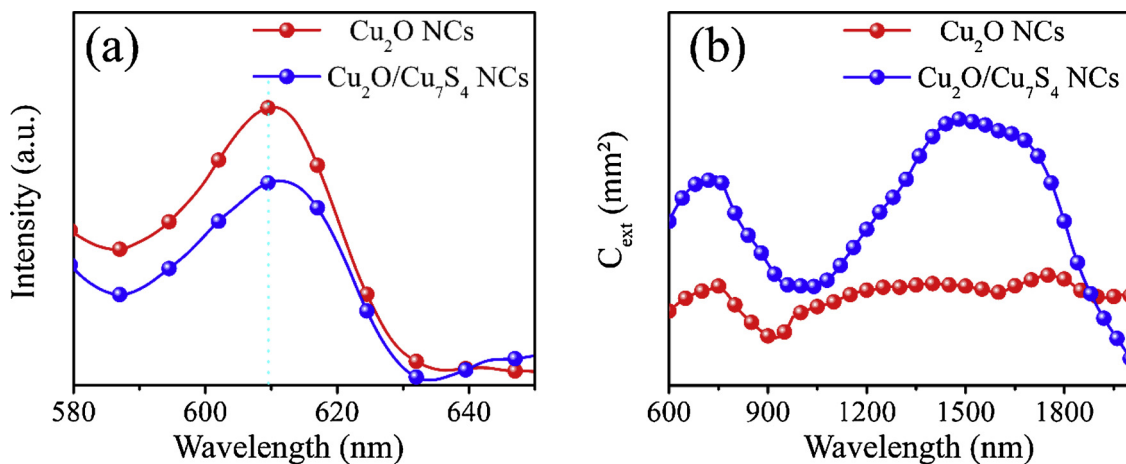

Fig. 5. (a) Photoluminescence spectra of Cu_2O and Cu_2O/Cu_7S_4 NCs with excitation spectra are 460 nm. (b) LSPR absorption spectra of Cu_2O and Cu_2O/Cu_7S_4 NCs obtained from NIR absorption.

H_2O oxidation to O_2 for PEC). In detail, such a charge transfer process in Cu_2O/Cu_7S_4 NCs enhances photogenerated electrons and holes separation and the lifetime of carriers. The enhanced lifespan contributes to the multielectron processes with kinetic restraints, so particularly important for photocatalytic HER. Otherwise, the presence of Cu_7S_4 with LSPR can enhance visible light absorption efficiency and accelerate electron transfer, also contribute to photocatalytic HER.

4. Conclusions

Cu_7S_4 as a cocatalyst and combined with Cu_2O in situ is first applied to photocatalytic HER. Cu_2O/Cu_7S_4 NCs exhibit highly efficient light-driven photocatalytic activity in HER as compared to Cu_2O NCs. The cocatalyst Cu_7S_4 could contribute to electron transfer as its well electricity, also benefit to light harvesting as the LSPR character, thus the photocurrent density and solar conversion efficiency increasing 1.5 and 1.114 times of Cu_2O/Cu_7S_4 compared to Cu_2O, respectively. Furthermore, the results indicate that the LSPR absorption of Cu_7S_4 in
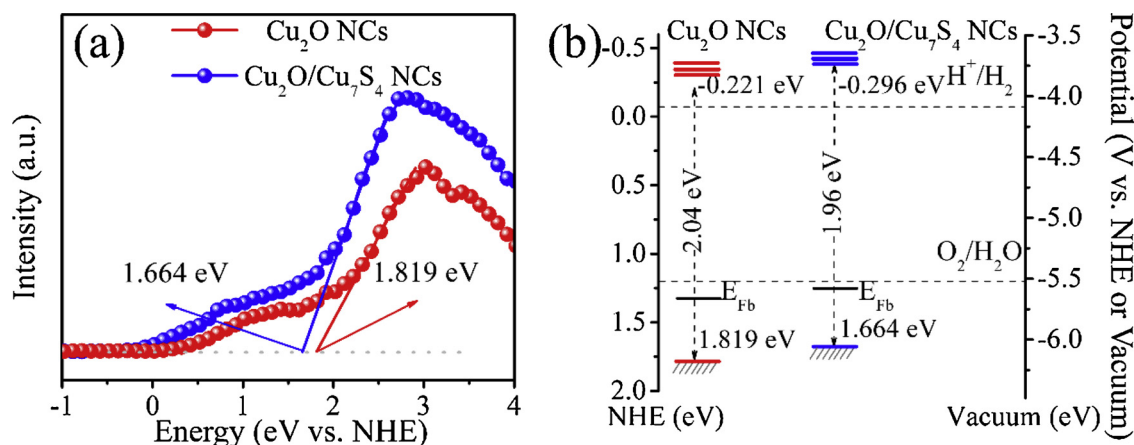
Fig. 6. Energy band characterizations and diagrams of Cu₂O and Cu₂O/Cu₇S₄ NCs: (a) Valence-band spectra obtained by XPS. (b) Schematic energy level diagrams in comparison with the potentials for water reduction and oxidation.
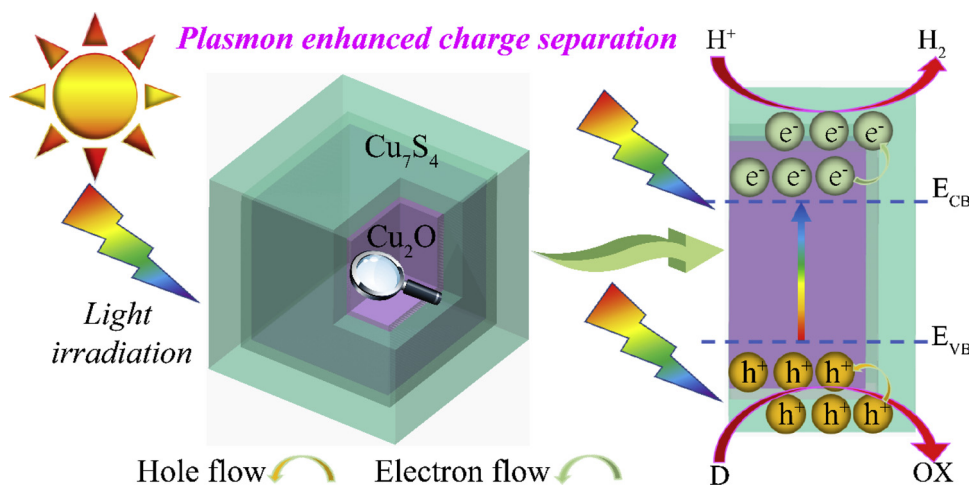

Fig. 7. Schematic illustration of the proposed mechanism for photocatalytic HER of Cu₂O/Cu₇S₄ NCs under light irradiation. The right part is the view of the left one in detail. "e⁻" and "h⁺" represent electron and hole, respectively. "D" and "OX" mean electron donor (Na₂SO₃ in our work) and oxidation products, respectively.

Cu_2O/Cu_7S_4 NCs also has significant contribution to the separation of photogenerated electron and holes, thus allowing the photogenerated electrons and holes to have enough time to participate the overall photocatalytic reactions. Therefore, high hydrogen production rate of $1689.00\,\mu mol g^{-1}h^{-1}$ can be gained for Cu_2O/Cu_7S_4 NCs. Finally, the strategy of the nanocrystals synthesized involving roxbyite Cu_7S_4 nanoparticles as a cocatalyst on a semiconductor surface and exploiting their LSPR for enhancing photocatalytic activities have considerable impact on the future development of highly efficient photocatalysts for water splitting.

Conflict of interest

The authors declare no competing financial interest.

Acknowledgements

Appendix A. Supplementary data

Supplementary material related to this article can be found, in the online version, at doi:https://doi.org/10.1016/j.apcatb.2019.01.042.

References

[1] J.P. Torella, C.J. Gagliardi, J.S. Chen, D.K. Bediako, B. Colon, J.C. Way, P.A. Silver, D.G. Nocera, Efficient solar-to-fuels production from a hybrid microbial-water-splitting catalyst system, Proc. Natl. Acad. Sci. U. S. A. 112 (2015) 2337–2342.

[2] A. Eftekhari, V.J. Babu, S. Ramakrishna, Photoelectrode nanomaterials for photo-electrochemical water splitting, Int. J. Hydrogen Energy 42 (2017) 11078–11109.

[3] S. Linic, P. Christopher, D.B. Ingram, Plasmonic-metal nanostructures for efficient conversion of solar to chemical energy, Nat. Mater. 10 (2011) 911–921.

[4] C.A. Downes, S.C. Marinescu, Efficient electrochemical and photoelectrochemical H₂ production from water by a cobalt dithiolene one-dimensional metal-organic surface, J. Am. Chem. Soc. 137 (2015) 13740–13743.

[5] A. Paracchino, V. Laporte, K. Sivula, M. Gratzel, E. Thimsen, Highly active oxide photocathode for photoelectrochemical water reduction, Nat. Mater. 10 (2011) 456–461.

[6] X. Liu, Z. Li, W. Zhao, C. Zhao, Y. Wang, Z. Lin, A facile route to the synthesis of reduced graphene oxide-wrapped octahedral Cu₂O with enhanced photocatalytic and photovoltaic performance, J. Mater. Chem. A Mater. Energy Sustain. 3 (2015) 19148–19154.

[7] Z. Lin, J. Xiao, L. Li, P. Liu, C. Wang, G. Yang, Nanodiamond-embedded p-type copper(I) oxide nanocrystals for broad-spectrum photocatalytic hydrogen evolution, Adv. Energy Mater. 6 (2016) 1501865.

[8] H. Liu, G. Zhao, X. Meng, J. Ye, Doping Ba into strontium titanate for enhanced photocatalytic oxygen evolution over its supported Au-based catalysts, Catal. Commun. 99 (2017) 127–130.

[9] E. Nurlaela, H. Wang, T. Shinagawa, S. Flanagan, S. Ould-Chikh, M. Qureshi, Z. Mics, P. Sautet, T. Le Bahers, E. Cánovas, M. Bonn, K. Takanabe, Enhanced kinetics of hole transfer and electrocatalysis during photocatalytic oxygen evolution by cocatalyst tuning, ACS Catal. 6 (2016) 4117–4126.

[10] E. Nurlaela, T. Shinagawa, M. Qureshi, D.S. Dhawale, K. Takanabe, Temperature dependence of electrocatalytic and photocatalytic oxygen evolution reaction rates using NiFe oxide, ACS Catal. 6 (2016) 1713–1722.

[11] G. Liu, P. Li, G. Zhao, X. Wang, J. Kong, H. Liu, H. Zhang, K. Chang, X. Meng,

T. Kako, J. Ye, Promoting active species generation by plasmon-induced hot-electron excitation for efficient electrocatalytic oxygen evolution, J. Am. Chem. Soc. 138 (2016) 9128–9136.

[12] J. Tian, H. Li, Z. Xing, L. Wang, Y. Luo, A.M. Asiri, A.O. Al-Youbi, X. Sun, One-pot green hydrothermal synthesis of CuO-Cu₂O-Cu nanorod-decorated reduced graphene oxide composites and their application in photocurrent generation, Catal. Sci. Technol. 2 (2012) 2227.

[13] L. Zhang, D. Jing, L. Guo, X. Yao, In situ photochemical synthesis of Zn-doped Cu₂O hollow microcubes for high efficient photocatalytic H₂ production, ACS Sustain. Chem. Eng. 2 (2014) 1446–1452.

[14] W.C. Huang, L.M. Lyu, Y.C. Yang, M.H. Huang, Synthesis of Cu₂O nanocrystals from cubic to rhombic dodecahedral structures and their comparative photocatalytic activity, J. Am. Chem. Soc. 134 (2012) 1261–1267.

[15] B. Wang, R. Li, Z. Zhang, W. Zhang, X. Yan, X. Wu, G. Cheng, R. Zheng, Novel Au/Cu₂O multi-shelled porous heterostructures for enhanced efficiency of photoelectrochemical water splitting, J. Mater. Chem. A Mater. Energy Sustain. 5 (2017) 14415–14421.

[16] L. Liu, Y. Qi, J. Hu, W. An, S. Lin, Y. Liang, W. Cui, Stable Cu₂O@g-C₃N₄ core@shell nanostructures: efficient visible-light photocatalytic hydrogen evolution, Mater. Lett. 158 (2015) 278–281.

[17] Q. Hua, D. Shang, W. Zhang, K. Chen, S. Chang, Y. Ma, Z. Jiang, J. Yang, W. Huang, Morphological evolution of Cu₂O nanocrystals in an acid solution: stability of different crystal planes, Langmuir 27 (2011) 665–671.

[18] Z. Zhang, R. Dua, L. Zhang, H. Zhu, H. Zhang, Peng Wang, Carbon-layer-protected cuprous oxide nanowire arrays for efficient water reduction, ACS Nano 7 (2013) 1709–1717.

[19] E. Asenath-Smith, J.M. Noble, R. Hovden, A.M. Uhl, A. DiCorato, Y.-Y. Kim, A.N. Kulak, F.C. Meldrum, L.F. Kourkoutis, L.A. Estrof, Physical confinement promoting formation of Cu₂O-Au heterostructures with Au nanoparticles entrapped within crystalline Cu₂O nanorods, Chem. Mater. 29 (2017) 555–563.

[20] S. Bao, H.A.N. Zhu, P.A.N. Wang, M. Zou, M. Du, M. Zhang, Template strategy for the synthesis of Cu₂O-Pt hierarchical heterostructures for the degradation of methylene blue, Nano: Brief Reports Rev. 08 (2013) 1350062.

[21] Z. Zhang, Z. Wang, S.-W. Cao, C. Xue, Au/Pt nanoparticle-decorated TiO₂ nanofibers with plasmon-enhanced photocatalytic activities for solar-to-fuel conversion, J. Phys. Chem. C 117 (2013) 25939–25947.

[22] S. Cao, Y. Chen, H. Wang, J. Chen, X. Shi, H. Li, P. Cheng, X. Liu, M. Liu, L. Piao, Ultrasmall CoP nanoparticles as efficient cocatalysts for photocatalytic formic acid dehydrogenation, Joule 2 (2018) 549–557.

[23] J. Zhou, Y. Liu, Z. Zhang, J. Li, X. Qi, CoSe₂ nanosheets decorated on carbon fibers as efficient and stable catalysts for hydrogen evolution reaction, J. Mater. Sci.-Mater. Electron. 29 (2018) 12300–12305.

[24] M.Z. Rahman, K. Davey, S.Z. Qiao, Carbon, nitrogen and phosphorus containing metal-free photocatalysts for hydrogen production: progress and challenges, J. Mater. Chem. A Mater. Energy Sustain. 6 (2018) 1305–1322.

[25] L. Wei, Y. Chen, Y. Lin, H. Wu, R. Yuan, Z. Li, MoS₂ as non-noble-metal cocatalyst for photocatalytic hydrogen evolution over hexagonal ZnIn₂S₄ under visible light irradiations, Appl. Catal. B: Environ. 144 (2014) 521–527.

[26] Q. Xiang, J. Yu, M. Jaroniec, Synergetic effect of MoS₂ and graphene as cocatalysts for enhanced photocatalytic H₂ production activity of TiO₂ nanoparticles, J. Am. Chem. Soc. 134 (2012) 6575–6578.

[27] J. Chen, X.-J. Wu, L. Yin, B. Li, X. Hong, Z. Fan, B. Chen, C. Xue, H. Zhang, One-pot synthesis of CdS nanocrystals hybridized with single-layer transition-metal dichalcogenide nanosheets for efficient photocatalytic hydrogen evolution, Angew. Chem. Int. Ed. 54 (2015) 1210–1214.

[28] Y. Hou, Y. Zhu, Y. Xu, X. Wang, Photocatalytic hydrogen production over carbon nitride loaded with WS₂ as cocatalyst under visible light, Appl. Catal. B: Environ. 156 (2014) 122–127.

[29] L. Xu, X. Deng, Z. Li, Photocatalytic splitting of thiols to produce disulfides and hydrogen over PtS/ZnIn₂S₄ nanocomposites under visible light, Appl. Catal. B: Environ. 234 (2018) 50–55.

[30] Y. Zhang, Z. Peng, S. Guan, X. Fu, Novel β-NiS film modified cds nanoflowers heterostructure nanocomposite: extraordinarily highly efficient photocatalysts for hydrogen evolution, Appl. Catal. B: Environ. 224 (2018) 1000–1008.

[31] Z. Wang, J. Peng, X. Feng, Z. Ding, Z. Li, Wide spectrum responsive CdS/NiTiO₃/CoS with superior photocatalytic performance for hydrogen evolution, Catal. Sci. Technol. 7 (2017) 2524–2530.

[32] J. Cui, Y. Li, L. Liu, L. Chen, J. Xu, J. Ma, G. Fang, E. Zhu, H. Wu, L. Zhao, L. Wang, Y. Huang, Near-infrared plasmonic-enhanced solar energy harvest for highly efficient photocatalytic reactions, Nano Lett. 15 (2015) 6295–6301.

[33] J.M. Luther, P.K. Jain, T. Ewers, A.P. Alivisatos, Localized surface plasmon resonances arising from free carriers in doped quantum dots, Nat. Mater. 10 (2011) 361–366.

[34] Y. Jiang, S. Zhang, Q. Ji, J. Zhang, Z. Zhang, Z. Wang, Ultrathin Cu₇S₄ nanosheets-

constructed hierarchical hollow cubic cages: one-step synthesis based on kirkendall effect and catalysis property, J. Mater. Chem. A Mater. Energy Sustain. 2 (2014) 4574–4579.

[35] J. Li, L. Sun, Y. Yan, Z. Zhu, A novel fabrication of Cu₂O@Cu₇S₄ core-shell micro/nanocrystals from Cu₂O temples and enhanced photocatalytic activities, Mater. Res. Bull. 80 (2016) 200–208.

[36] X. Yu, J. Bi, G. Yang, H. Tao, S. Yang, Synergistic effect induced high photothermal performance of Au nanorod@Cu₇S₄ yolk-shell nanooctahedron particles, J. Phys. Chem. C 120 (2016) 24533–24541.

[37] Y. Dai, X. Zhu, H. Liu, Y. Lin, W. Sun, Y. Sun, C. Ding, C. Luo, Q. Wei, Morphology-dependent electrochemical behavior of 18-facet Cu₇S₄ nanocrystals based electrochemical sensing platform for hydrogen peroxide and prostate specific antigen, Biosens. Bioelectron. 112 (2018) 143–148.

[38] F. Tao, Y. Zhang, F. Zhang, K. Wang, X. Chang, Y. An, L. Dong, Y. Yin, From CdS to Cu₇S₄ nanorods via a cation exchange route and their applications: environmental pollution removal, photothermal conversion and light-induced water evaporation, ChemistrySelect 2 (2017) 3039–3048.

[39] J. Xu, J. Cui, C. Guo, Z. Zhao, R. Jiang, S. Xu, Z. Zhuang, Y. Huang, L. Wang, Y. Li, Ultrasmall Cu₇S₄@MoS₂ hetero-nanoframes with abundant active edge sites for ultrahigh-performance hydrogen evolution, Angew. Chem. Int. Ed. 55 (2016) 6502–6505.

[40] Q. Yuan, D. Liu, N. Zhang, W. Ye, H. Ju, L. Shi, R. Long, J. Zhu, Y. Xiong, Noble-metal-free janus-like structures by cation exchange for z-scheme photocatalytic water splitting under broadband light irradiation, Angew. Chem. Int. Ed. 56 (2017) 4206–4210.

[41] H. Bao, Z. Zhang, Q. Hua, W. Huang, Compositions, structures, and catalytic activities of CeO₂@Cu₂O nanocomposites prepared by the template-assisted method, Langmuir 30 (2014) 6427–6436.

[42] H.L. Wu, R. Sato, A. Yamaguchi, M. Kimura, M. Haruta, H. Kurata, T. Teranishi, Formation of pseudomorphic nanocages from Cu₂O nanocrystals through anion exchange reactions, Science 351 (2016) 1306–1310.

[43] S. Jiao, L. Xu, K. Jiang, D. Xu, Well-defined non-spherical copper sulfide mesocages with single-crystalline shells by shape-controlled Cu₂O crystal templating, Adv. Mater. 18 (2006) 1174–1177.

[44] L. Yu, G. Li, X. Zhang, X. Ba, G. Shi, Y. Li, P.K. Wong, J.C. Yu, Y. Yu, Enhanced activity and stability of carbon-decorated cuprous oxide mesoporous nanorods for CO₂ reduction in artificial photosynthesis, ACS Catal. 6 (2016) 6444–6454.

[45] W. Niu, T. Moehl, W. Cui, R. Wick-Joliat, L. Zhu, S.D. Tilley, Extended light harvesting with dual Cu₂O-based photocathodes for high efficiency water splitting, Adv. Energy Mater. 8 (2018) 1702323.

[46] Y. Zhao, C. Wang, G.G. Wallace, Tin nanoparticles decorated copper oxide nanowires for selective electrochemical reduction of aqueous CO₂ to CO, J. Mater. Chem. A Mater. Energy Sustain. 4 (2016) 10710–10718.

[47] Z. Li, Z. Zhang, Tetrafunctional Cu₂S thin layers on Cu₂O nanowires for efficient photoelectrochemical water splitting, Nano Res. 11 (2018) 1530–1540.

[48] Z. Li, Y. Xin, Z. Zhang, New photocathodic analysis platform with quasi-core/shell-structured TiO₂@Cu₂O for sensitive detection of H₂O₂ release from living cells, Anal. Chem. 87 (2015) 10491–10497.

[49] L. Meng, D. Rao, W. Tian, F. Cao, X. Yan, L. Li, Simultaneous manipulation of O-doping and metal vacancy in atomically thin Zn₁₀In₁₆S₃₄ nanosheet arrays toward improved photoelectrochemical performance, Angew. Chem. Int. Ed. 57 (2019) 16882–16887, https://doi.org/10.1002/ange.201811632.

[50] Z. Chen, D. Cummins, B.N. Reinecke, E. Clark, M.K. Sunkara, T.F. Jaramillo, Core-shell MoO₃-MoS₂ nanowires for hydrogen evolution: a functional design for electrocatalytic materials, Nano Lett. 11 (2011) 4168–4175.

[51] X.Q. Chen, Z. Li, Y. Bai, Q. Sun, L.Z. Wang, S.X. Dou, Room-temperature synthesis of Cu(2-x)E (E = S, Se) nanotubes with hierarchical architecture as high-performance counter electrodes of quantum-dot-sensitized solar cells, Chem.-Eur. J. 21 (2015) 1055–1063.

[52] X.-H. Zhang, N. Li, J. Wu, Y.-Z. Zheng, X. Tao, Defect-rich O-incorporated 1T-MoS₂ nanosheets for remarkably enhanced visible-light photocatalytic H₂ evolution over CdS: the impact of enriched defects, Appl. Catal. B: Environ. 229 (2018) 227–236.

[53] P. Wang, Y. Sheng, F. Wang, H. Yu, Synergistic effect of electron-transfer mediator and interfacial catalytic active-site for the enhanced H₂-evolution performance: a case study of CdS/Au photocatalyst, Appl. Catal. B: Environ. 220 (2018) 561–569.

[54] T. Jiang, T. Xie, L. Chen, Z. Fu, D. Wang, Carrier concentration-dependent electron transfer in Cu(II)O/ZnO nanorod arrays and their photocatalytic performance, Nanoscale 5 (2013) 2938–2944.

[55] C. Li, Y. Li, J.-J. Delaunay, A novel method to synthesize highly photoactive Cu₂O microcrystalline films for use in photoelectrochemical cells, ACS Appl. Mater. Inter. 6 (2014) 480–486.

[56] S.K. Saraswat, D.D. Rodene, R.B. Gupta, Recent advancements in semiconductor materials for photoelectrochemical water splitting for hydrogen production using visible light, Renew. Sust. Energy Rev. 89 (2018) 228–248.